ISSN: 1687-1006 p
ISSN: 2682-3640 e

The Egyptian International Journal of Engineering Sciences and Technology

https://eijest.journals.ekb.eg/

Vol. 51 (2025) 64–79

DOI: 10.21608/eijest.2025.333926.1303

Computational Optimization of Wind Turbine Winglets for Enhanced Energy Capture

Akrm Abaza[a]*, Ahmed Farouk AbdelGawad[a], and Mahmoud Ahmed[b]

[a]*Mechanical Power Engineering Department, Faculty of Engineering, Zagazig University, Zagazig, Egypt*
[b]*Department of Mechanical Engineering, Egyptian Academy for Engineering and Advanced Technology, Cairo, Egypt*

ARTICLE INFO

Article history:

Received 05 November 2024
Received in revised form 05 January 2025
Accepted 05 January 2025
Available online 05 January 2025

Keywords:

1st Wind turbine
2nd CFD
3th winglet
4th renewable sources
5th energy

ABSTRACT

With international strength demands rapidly growing, enhancing the performance of renewable strength structures is critical. This study at investigates the aerodynamic optimization of wind mills through the mixing of winglets—vertical extensions at blade hints—to enhance power capture. Using computational fluid dynamics (CFD) simulations and experimental validation, the consequences of winglet geometry and blade pitch attitude on turbine performance had been analyzed. The ultimate winglet layout, presenting a 4% blade period, a 45° can't perspective, and a 50% top radius of curvature, extended the energy coefficient (C_p) via 17.36% as compared to the baseline blade without winglets. Additionally, optimum pitch angles of 50° at wind speeds of 7.2 m/s and 9 m/s maximized energy output, reaching increases of 33.4 W and 83.2 W, respectively. The CFD consequences established decreased tip vortex strength and stepped forward aerodynamic overall performance with winglet integration, tested by way of experimental wind tunnel tests. These findings make a contribution to the improvement of next-era wind turbines with improved performance and electricity output.

1. INTRODUCTION

Winglets have emerged as a promising technology for enhancing the aerodynamic efficiency of wind turbines in recent years. Winglets refer to vertical aerodynamic devices fixed to the tips of wind turbine blades, analogous to wingtip extensions used in aviation to optimize airflow and reduce induced drag as given in [1]. However, effectively harnessing the performance benefits of winglets requires specialized multidisciplinary design optimization accounting for intricate fluid-structure interactions along the blade.
Recent computational fluid dynamics (CFD) simulations have provided initial insights into the impacts of winglets on wind turbine blade aerodynamics and performance. In a detailed CFD study, various winglet designs on a 13 MW offshore wind turbine were tested in [2]. Their parametric analysis found that a winglet with 15% blade length and 60° cant angle increased annual energy production by 1.2% compared to the baseline blade without a winglet. In contrast, winglets on a smaller 1 MW horizontal-axis wind turbine were evaluated in [3] and noted negligible gains in terms of power output. The discrepancies across these studies highlight the importance of custom winglet design optimization

* *Corresponding author. Tel.:+2 01098199431*
E-mail address: akrammabaza@gmail.com

based on the specific turbine scale, rotor diameter, blade geometry, and operating conditions.

A few experimental validations have also started to emerge to supplement the computational studies. For instance, blades with curved and tapered winglets for a 20 kW horizontal-axis wind turbine were designed and manufactured using vacuum infusion molding techniques as shown in [4]. Controlled wind tunnel testing revealed a 7% increase in power output compared to the original blade without winglets. However, physical experiments remain limited, indicating the need for more robust field testing across turbine scales to truly verify the simulated performance improvements.

Beyond passive winglet designs, researchers have also explored innovations in active flow control and morphing winglet concepts. A smart morphing winglet for wind turbine blades was using shape memory alloy actuators that could dynamically adjust the cant angle and curvature based on operating conditions as given in [5]. Wind tunnel tests demonstrated a 12% increase in power output at low wind speeds by optimally adapting the winglet geometry in real-time. Such active flow control presents a novel frontier for further enhancing winglet aerodynamic benefits

While power output improvements from winglets appear promising, potential downsides such as increased weight, noise, and manufacturing costs require careful evaluation when implementing winglets as shown in [6]. Overall, winglets show strong potential for augmenting wind turbine performance but necessitate multidisciplinary design optimization frameworks and more extensive field testing across turbine scales to translate simulated aerodynamic gains into improved annual energy production for commercial wind farms.

2. BLADE DESIGN

The blade geometry was designed using the SolidWorks computer-aided design software based on the NACA (National Advisory Committee for Aeronautics) 4418 airfoil. NACA airfoils are shaped to optimize aerodynamic flow and are commonly used in wind turbine applications as given in [7]. The NACA 4418 is a four-digit airfoil with a 18% maximum camber located 40% downstream from the leading edge as given in [8].

Table 1. Blade design specifications along the radius

Section NO.	1	2	3	4	5	6	7	8	9	10
R (m)	0.2	0.4	0.6	0.8	1	1.2	1.4	1.6	1.8	2
Pitch angle ('deg')	30.1	21.9	13.7	8.8	5.8	3.9	2.8	1.8	0	0
Chord length (m)	0.33	0.56	0.61	0.54	0.47	0.42	0.38	0.35	0.32	0.3

Table 1 presents the specifications along the blade radius. The blade was divided into 10 sections along the radial (R) direction. R represents the radial distance from the rotor hub center at which the blade section is located, measured in meters (m) as shown in [9]. The radius essentially describes the spanwise position along the blade, from root to tip. Specifying the pitch angle, chord length, and other parameters as a function of R enables optimization of the blade geometry at different radial stations. This spanwise tailoring of the design aims to maximize aerodynamic performance and structural integrity across operating conditions. The pitch angle was varied from root to tip, decreasing from 30.15° to 0°. The chord length (airfoil width) tapered from 0.33 m at the root to 0.3 m at the tip. These optimized distributions aim to maximize aerodynamic performance across operating conditions as shown in [10].

Fig. 1. Airfoil for every section with Twist angle

Figure 1 shows the blade design airfoil profiles at different radial sections along the blade span. As indicated in Table 1, the blade geometry utilizes the NACA 4418 airfoil shape. This airfoil contour is maintained along the entire length of the blade, from root to tip. However, the pitch angle (twist) is varied at each section as per the specifications in Table 1.

This spanwise twist distribution aims to optimize the local angle of attack seen by each blade section for improved aerodynamic performance as illustrated in [11]. At the inner regions closer to the hub, higher twist angles help avoid flow separation at the low rotational speeds. Moving towards the tip, the twist angle is reduced since the higher rotational velocities generate adequate lift even at lower angles of attack. This helps reduce drag. Therefore, tailoring the twist

angle along the radius aims to enhance efficiency across the operating regime from low to high wind speeds.

The chord length also reduces slightly from root to tip as per Table 1. This tapered planform contributes to a lighter blade weight towards the tip. Together, the spanwise variations in airfoil camber, chord, and twist angle enable customization of the blade for optimized structural integrity and aerodynamic performance.

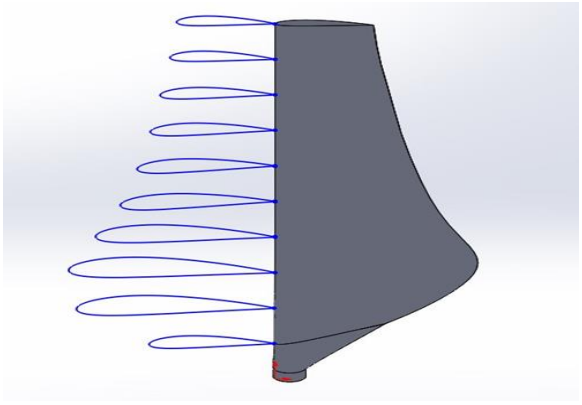

Fig. 2. 3D Blade after loft

Figure 2 shows the final 3D model of the wind turbine blade generated through a lofting procedure in SolidWorks. The 2D NACA 4418 airfoil profiles depicted in Figure 1 were extruded and smoothly connected along the span to create the 3D geometry. As illustrated in the figure, the blade twists from root to tip as per the pitch angle specifications in Table 1. Additionally, the chord length can be observed reducing towards the tip according to the tapering chord distribution in Table 1.

This lofting process enables translation of the 2D airfoil shape and pitch/chord distributions into a fully 3D model incorporating the desired spanwise variations. The smooth contours and aerodynamic profile of the resulting blade aim to optimize wind energy extraction. The wider chord and high twist at the root provide strength and stiffness to support the blade weight, while the thinner and untwisted tip minimizes drag during rotation. This tailored 3D geometry based on the design parameters in Table 1 is analyzed using computational fluid dynamics to evaluate aerodynamic forces and resulting structural loads. The analysis provides feedback to refine the blade shape for performance optimization.

The objective of the present work is to investigate the impact of winglet integration on wind turbine blade performance and energy capture. This study combines computational fluid dynamics (CFD) simulations and experimental validation to analyze the aerodynamic benefits of adding winglets to wind turbine blades. Key parameters tested in the investigation include winglet geometries—specifically height, cant angle, and radius of curvature—along with blade pitch angles and varying wind speeds. By evaluating these factors, the study aims to optimize winglet design and pitch control to enhance power output, improve aerodynamic efficiency, and reduce energy losses caused by tip vortices.

2.1. Power Calculation

The parameters used for the design of wind turbine can be expressed by the following equations.

$$\boldsymbol{\lambda_r = \frac{r}{R} * \lambda} \qquad (1)$$

Where,

$\boldsymbol{\lambda_r}$ is local speed ratio.

R is blade radius.

r is the section radius.

This calculates the local speed ratio (λ_r) at a given blade radius (r) based on the tip speed ratio (λ_r) and total blade radius (R) [12].

$$\boldsymbol{\emptyset = \frac{2}{3} tan^{-1} * \left(\frac{1}{\lambda_r}\right)}, \qquad (2)$$

Where,

Ø is angle of relative wind.

λ_r is local speed ratio.

This determines the relative wind angle (Ø) seen by the blade section using the inverse tangent of the local speed ratio (λ_r) [13].

$$\boldsymbol{\emptyset_{degree} = \frac{2}{3} tan^{-1} * \left(\frac{1}{\lambda_r}\right) * \frac{180}{\pi}} \qquad (3)$$

Converts the relative wind angle (Ø) in radians to degrees

$$\boldsymbol{C_i = \frac{8 * \pi\, r}{B * Cl}\left(1 - cos(\emptyset)\right)}, \qquad (4)$$

where,

$\boldsymbol{C_i}$ is Local chord length at a blade section.

B is Number of blades.

C_l is Lift coefficient of the airfoil section.

Ø is Relative wind angle in radians.

$$\boldsymbol{\theta_p = (\emptyset - \alpha)}, \qquad (5)$$

where,

$\boldsymbol{\theta_p}$ is section pitch angle, between cord line and plane of rotation.

Ø is angle of relative wind.

$\boldsymbol{\alpha}$ is angle of attack.

Calculates the section pitch angle (θ_p) by subtracting the angle of attack (α) from the relative wind angle (Ø) as given in [12].

$$\boldsymbol{\theta_{p\,degree} = (\emptyset - \alpha) * \frac{180}{\pi}} \qquad (6)$$

Converts the section pitch angle ($\theta_{p\,degree}$) from radians to degrees.

$$\boldsymbol{\emptyset_T = \frac{2}{3} \tan^{-1} \frac{1}{\lambda}}, \qquad (7)$$

where,
$\emptyset_T$ is blade twist angle.
λ is rotor radius.
Calculates the pitch angle at the tip (θ_{p°) by subtracting the angle of attack (α) from the twist angle ($\emptyset_T$) [12].
Determines the blade twist angle ($\emptyset_T$) at the tip based on the inverse tangent of the tip speed ratio (λ) [13].

$$\theta_{p^\circ} = (\emptyset_T - \alpha), \quad (8)$$

where,
θ_{p° is blade pitch angle at tip.
$\emptyset_T$ is blade twist angle.
α is angle of attack.
Calculates the pitch angle at the tip (θ_{p°) by subtracting the angle of attack (α) from the twist angle ($\emptyset_T$) [12].

$$\theta_T = \theta_p - \theta_{p^\circ}, \quad (9)$$

where,
θ_T is Span-wise twist angle distribution along the blade.
θ_p is Local pitch angle at a given blade section.
θ_{p° is Pitch angle specifically at the blade tip.
Determines the span-wise twist angle distribution (θ_T) by subtracting the tip pitch angle (θ_{p°) from the local pitch angle (θ_p).

$$\theta_T = (\theta_p - \theta_{p^\circ}) * \frac{180}{\pi} \quad (10)$$

Converts the twist angle distribution (θ_T) to degrees.

$$f = \frac{B}{2} * \frac{R - r}{r \sin\theta}, \quad (11)$$

where,
f is the correction factor.
The Prandtl tip loss factor (f) accounts for the loss in lift near the blade tip as shown in [12].

$$F = \frac{2}{\pi} \cos^{-1}(e^{-f}), \quad (12)$$

where,
F is a function of the number of blades.
The F function adjusts for the number of blades (B) using the Prandtl factor (f).

$$\sigma = \frac{C_i * B}{2\pi r}, \quad (13)$$

where,
σ is solidity.
Calculates the solidity (σ), which is the ratio of blade area to swept area as shown in [13].

$$a = \frac{\sigma r\, Cn}{(4 \sin\emptyset^4) + \sigma r\, Cn}. \quad (14)$$

Determines the axial induction factor (a) based on solidity, relative wind angle, and normal force coefficient (Cn) [12].

$$\acute{a} = \frac{\sigma r\, Cn}{(4 \sin\emptyset \cos\emptyset) - \sigma r\, Cn}. \quad (15)$$

Calculates the angular induction factor (a') using similar parameters as the axial induction factor (a) as given in [13].

$$C_n = C_l \cos\emptyset + C_d \sin\emptyset. \quad (16)$$

Resolves normal (C_n) and tangential (Ct) force coefficients from lift (Cl) and drag (Cd) coefficients.

$$C_t = C_l \sin\emptyset - C_d \cos\emptyset. \quad (17)$$

Resolves normal (C_n) and tangential (C_t) force coefficients from lift (C_l) and drag (C_d) coefficients

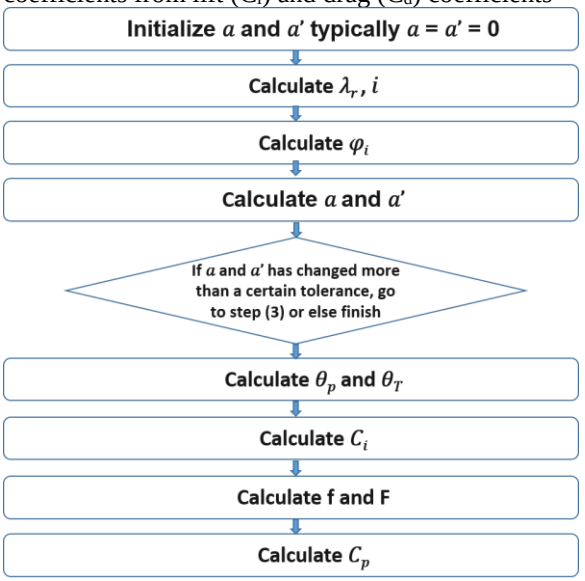

Fig. 3. Flow chart of Power

Blade element momentum (BEM) theory combines blade element theory and momentum theory to evaluate the aerodynamics of horizontal-axis wind turbines (HAWTs) as shown in [14]. This hybrid approach allows for the analysis of blade forces and induced velocities in greater detail. In BEM, the turbine blade is discretized into small elements along the radial direction. The forces on each blade section are analyzed individually using principles from both blade element theory and momentum theory. Blade element theory is used to estimate the local aerodynamic forces, while momentum theory accounts for induced velocity effects from the rotor wake.
First, the local velocity ratios, relative wind angles, pitch angles, and twist angle distributions are calculated along the blade based on the tip speed ratio and geometry (Eqs. 1-10). These parameters

determine the effective angle of attack seen at each section. Then, using sectional airfoil data, the normal and tangential force coefficients are found for each segment (Eqs. 16-17).

Momentum theory is applied to iteratively solve for the axial and tangential induction factors, which represent the velocity deficits in the wake (Eqs. 14-15). The induction factors account for the rotational effects induced by the rotor. They are used to modify the local inflow velocities from the upstream wind speed. With the induction factors, force coefficients, and adjusted velocities known, the sectional blade forces are integrated along the blade. The Prandtl tip loss model (Eqs. 11-12) is used to account for the decrease in forces near the tip due to vortex shedding. Finally, the integrated sectional forces are combined to determine the overall thrust, torque, and power for the complete rotor. This provides performance predictions that account for both the local airfoil aerodynamics and global wake induction effects.

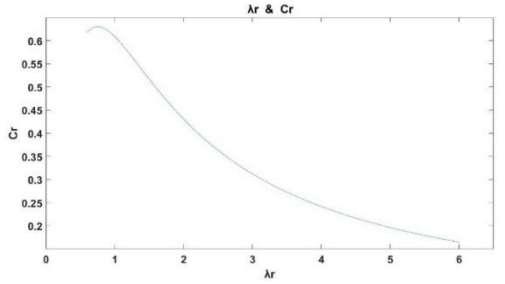

Fig. 4. Relation between λ_r and C_r

Figure 4 shows the inverse relationship between λ_r and C_r. As local speeds increase along the span, the blade tapers to a smaller chord. This improves the lift-to-drag ratio and rotors efficiency across the full range of Operational speeds.

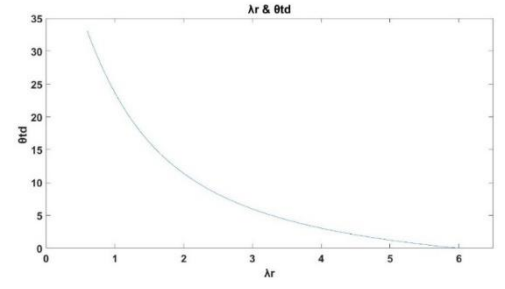

Fig. 5. Relation between λ_r and θt_d

Figure 5 shows the inverse relationship between local speed ratio (λ_r) and twist angle from root to tip of the blade. As the local speed ratio increases towards the tip, the twist angle decreases. This helps optimize the angle of attack seen at each section for lift generation. The higher twist angle near the root increases angle of attack at lower rotating speeds. Decreasing twist near the faster moving tip prevents stall at higher speeds.

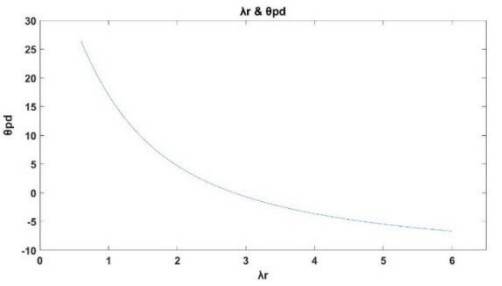

Fig. 6. Relation between λ_r and θp_d

Illustrates the relationship between the tip-speed ratio ($\boldsymbol{\lambda_r}$) and blade pitch angle ($\boldsymbol{\theta p_d}$), highlighting their impact on wind turbine performance. At low λ_r, θpd is reduced to maximize lift, while at high λ_r, θpd increases to limit drag and prevent overloading. This balance ensures optimal efficiency and structural safety..

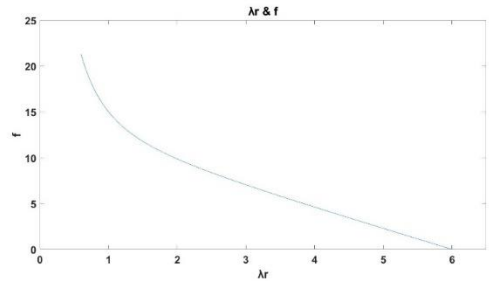

Fig. 7. Relation between λ_r and f

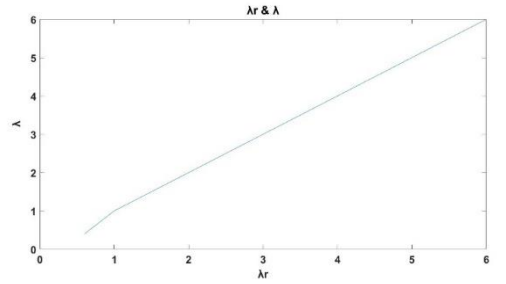

Fig. 8. Relation between λ_r and λ

Figures 7 and 8 illustrate how the lift and drag coefficients vary with angle of attack. The lift initially increases linearly then drops off after stalling. The drag coefficient rises steadily. Optimal angles of attack are chosen to maximize lift while minimizing drag.

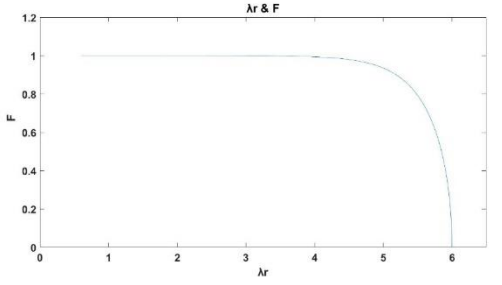

Fig. 9. Relation between λ_r and F

Figure 9 demonstrates how the optimal chord length and thickness are tailored from root to tip. The root utilizes a thicker airfoil to provide structural strength, while the tip can use a thinner section optimized for better lift-to-drag ratio.

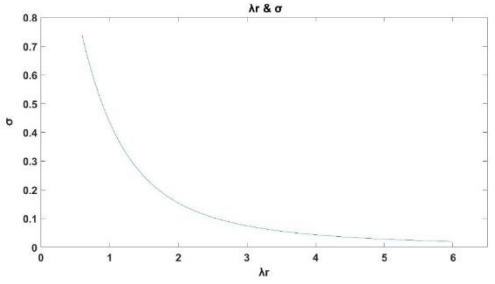

Fig. 10. Relation between λ_r and σ

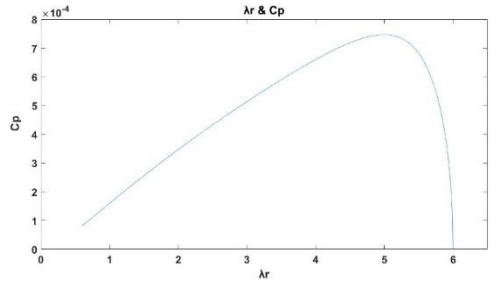

Fig. 11. Relation between λ_r and C_p

Figure 10 shows the relationship between the tip-speed ratio (**λ_r**) and solidity (**σ**), where increasing λ_r reduces σ, improving aerodynamic efficiency by lowering drag. **Figure 11** illustrates the relationship between **λ_r** and the power coefficient (**C_p**), with C_p peaking at the optimal λ_r, maximizing energy extraction efficiency.

2.2. Design of the Winglet

Winglet parameter was chosen according to the best performance using MATLAB.
Height = 4 % R, Cant angle =45◦, Radius of curvature = 50 % Height

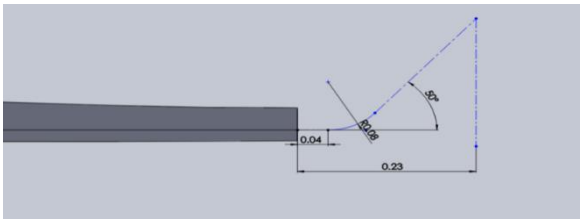

Fig. 12. Parameters for Winglet

Fig. 13. Blade with Winglet

Figure 12 illustrates the key parameters of the winglet, including its height, cant angle, and curvature, which were optimized to reduce vortex-induced drag and improve aerodynamic efficiency. These parameters were integrated into the wind turbine blade design. Figure 13 & 14 display a 3D model of the full wind turbine assembly created using SolidWorks CAD software. The major components clearly visible are the rotor blades with attached winglets, the nacelle housing the generator and drivetrain the base foundation. Color-coding of the different sections helps visualize how the modular wind turbine system fits together. The pictorial representation effectively communicates the real-world scale and configuration of the proposed wind turbine design with integrated winglets.

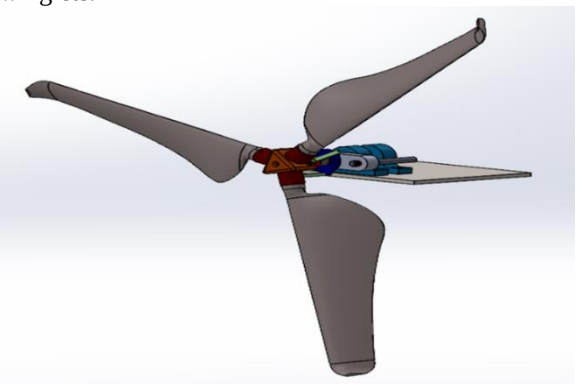

Fig.14. Wind turbine assembly in Solid-works

3. CFD SIMULATION

3.1. Meshing

Meshing is a critical step in computational fluid dynamics (CFD) modelling to discretize the model geometry into a grid of small cells or elements prior to simulation. Several meshing techniques were utilized to ensure good mesh quality for the wind turbine blade model.
First, a face match control was applied to the 120 degree blade segment to create a full 360 degree symmetric model. Face sizing controls were then used to set appropriate element sizes on key surfaces. Inflation layers were added to accurately capture boundary layer flow, with 15 layers on the blade and 5 layers on the interior. Finally, body sizing controls

set the element size within the volume, and an additional inflation layer was added to the blade tip.

3.2. Final Mesh Result

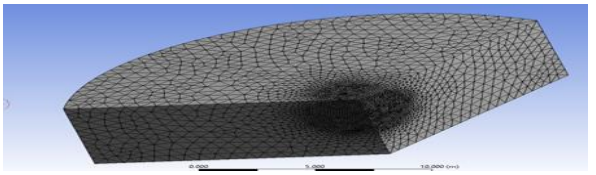

Fig. 15. Final Mesh 1

Figure 15 shows the resulting high quality structured mesh on the surface of the blade. The fine edge sizing and large number of inflation layers are clearly visible. Figure 16 displays a cutaway view revealing the volume mesh inside the blade. The gradual growth in element size from blade surface to interior is apparent, following best practices for aerodynamic analyses.

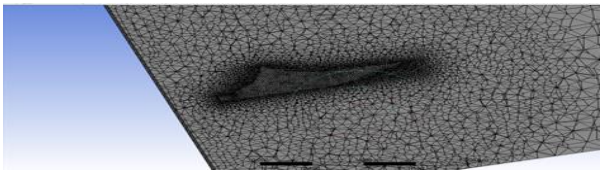

Fig. 16. Final Mesh 2

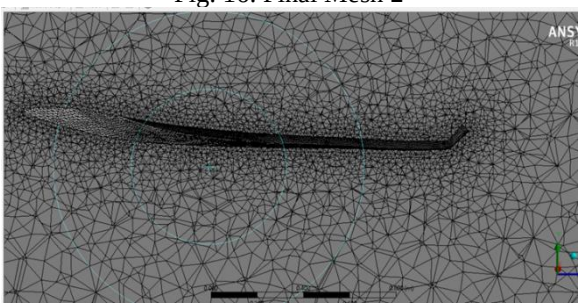

Fig. 17. Final Mesh 3

Figure 17 presents a close-up view of the mesh near the blade tip. A size gradation is evident in the volume mesh transitioning from fine elements near the surface to coarser in the interior. The tip inflation layer contains tightly packed prismatic elements to resolve flow in this critical region.

3.3 Results of CFD Simulations

ANSYS Fluent v18.2 is used to predict the aerodynamic performance of the wind turbine blade design. Convergence of the solution was assessed by monitoring the residual errors in the calculations.

Figure 18 shows the residual plots for continuity, velocity, and turbulence parameters k and epsilon over the iterations as given in [15]. The residuals represent the imbalance in the discretized flow equations, so they decrease as the solution converges as shown in [16]. A tolerance of 10^{-6} was set for all residuals to ensure a high level of convergence as shown in [17].

The residual values can be seen rapidly decreasing over the initial iterations before levelling off around 10^{-6} .This demonstrates that conservation of mass, momentum, and turbulence properties were satisfied to a tight tolerance as shown in [18], providing confidence in the accuracy of the CFD results. Most engineering applications specify a tolerance of 10^{-4}, but a tighter 10^{-6} criterion was used here to reduce numerical errors and obtain highly precise aerodynamic predictions for the blade design as shown in[19].

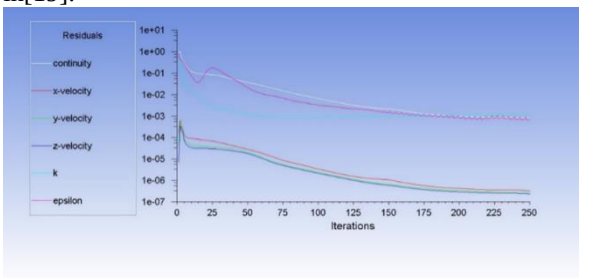

Fig. 18. Residuals

3.3.1. Results without winglet

The post-processing was done by using CFD-Post, which is the results visualization engine integrated in ANSYS Workbench. This comprehensive program allows to obtain contour plots, vector plots, streamlines and many other plots for computational fluid dynamics simulations. Other similar software in this category includes Tec plot and Para View

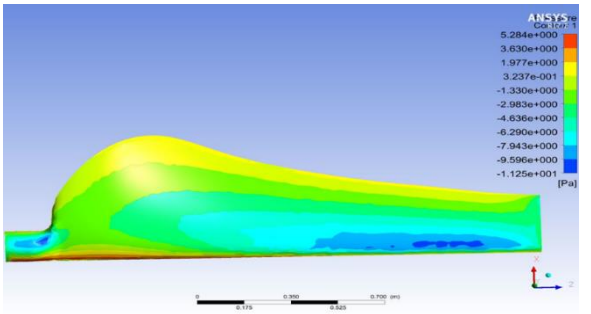

Fig. 19. Pressure contour-plot on back side

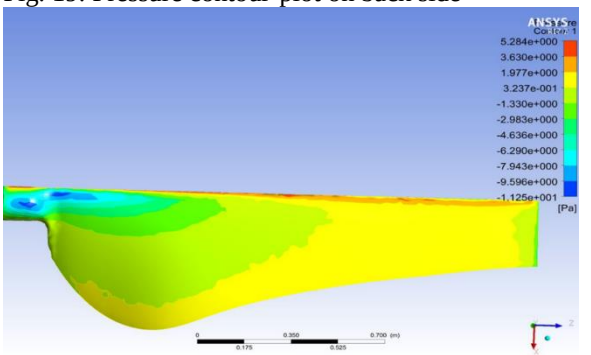

Fig. 20. Pressure contour-plot on top side

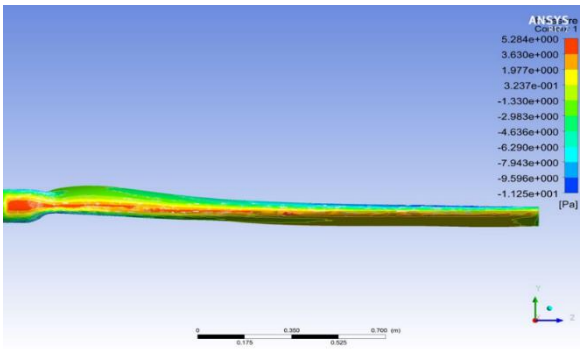

Fig. 21. Pressure on the leading edge of the blade

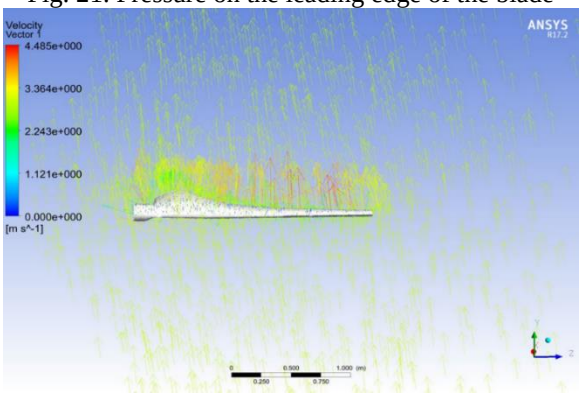

Fig. 22. Velocity Streamline

Several informative plots were created to analyse the airflow and pressures on the wind turbine blade. Figure 19 shows a pressure contour on the back/suction side of the blade. A region of low pressure near the leading edge and high pressure toward the trailing edge is observed, generating lift. While Figure 20 presents the pressure contour on the top/pressure side. Higher pressures are seen over most of this surface.

As well as, Figure 21 focuses on the leading edge pressures. The stagnation point and localized peak pressure on the leading edge are apparent. Finally Figure 22 depicts velocity streamlines traveling over the blade tip. The streamlines illustrate the airflow behavior and tip vortex generated as given in [21].

The coefficient of power for the baseline blade without winglet was determined from the simulation to be $C_p = 0.3013$. This was calculated using the equation:

$$\boldsymbol{C_p = P/(0.5 * \rho * A * v^3)}, \qquad (18)$$

where P is power, ρ is air density, A is rotor area, and v is wind velocity as shown in [22].

3.3.2. Results with winglet

Similarly, for the results with winglet

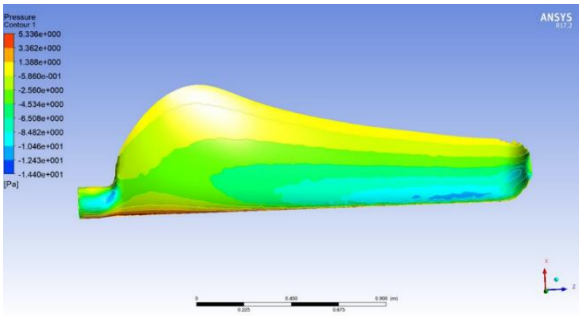

Fig. 23. Pressure contour plot on top side

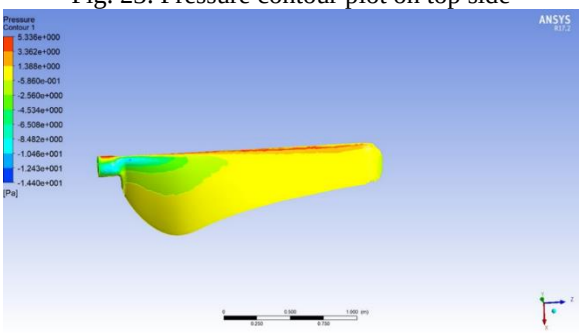

Fig. 24. Pressure contour plot on back side

The CFD results for the baseline blade with winglets provide insights into the flow behaviour and pressure distribution.

Figure 23 shows the pressure contour on the top surface of the blade. A region of high pressure is observed towards the leading edge. Figure 24 presents the pressure contour on the back side of the blade. There is an area of lower pressure near the leading edge on this side. Examination of the flow near the blade tip reveals the presence of a tip vortex, as expected in [13]. Figure 25 shows this vortex being shed from the blade tip and convecting downstream. The vortex velocity is approximately 3.36 m/s. Tip vortices generate undesirable drag on the blade.

For the winglet blade, the expectation was to see a reduction in the strength and size of the tip vortex. Winglets are designed to weaken vortices and displace them farther from the blade tip, decreasing drag. Figure 26 focuses on the leading edge pressures for the winglet blade. Here, an increase in pressure differential is observed compared to the baseline. This is attributed to the winglet's modification of the tip flow conditions and vortex behaviour.

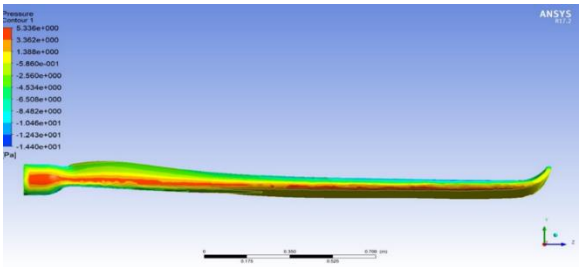

Fig. 25. Pressure on the leading edge of the blade

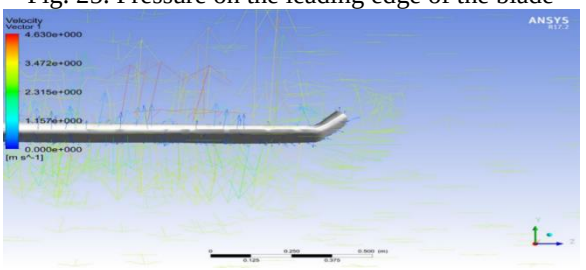

Fig. 26. Vortices around the tip of the blade

A key vector velocity plot of the flow downstream of the blade tip with the winglet addition. In contrast to the baseline case, the tip vortex appears split into two smaller vortices that are displaced from the blade tip. One vortex has been shifted outward away from the blade surface. The velocity in the modified tip flow field is slightly higher at approximately 3.472 m/s.

This altered vortex behaviour and increased velocity matches expectations for the impact of winglets. By disrupting the tip vortex formation, the winglets help reduce the strength of the swirling flow and move it farther from the blade. This is intended to decrease the undesirable induced drag caused by the tip vortices that would otherwise form.

The winglet design effectively achieved the goal of diminishing the tip vortex size and strength compared to the baseline blade without winglets. The changed flow physics quantified by the CFD analysis provide evidence that the concept of adding winglets for aerodynamic performance enhancement was successful. This demonstrates the value of high-fidelity CFD modelling for evaluating and optimizing wind turbine blade designs.

Table 2. Effect of Winglet Cant Angle on Wind Turbine Performance

Angle (deg)	Density of air (kg/m3)	Velocity (m/s)	Torque (N.m)	Cp
15	1.23	3	4.05	0.32
20	1.23	3	4.04	0.32
25	1.23	3	4.03	0.33
30	1.23	3	4.02	0.33
35	1.23	3	4.01	0.34
40	1.23	3	3.99	0.34
45	1.23	3	3.98	0.35
50	1.23	3	3.94	0.35
55	1.23	3	3.87	0.35

This table summarizes the impact of varying the winglet cant angle on the simulated torque and power coefficient of the wind turbine blade. The winglet cant angle is the angle at which the winglet is inclined relative to the blade plane. The ranges of cant angles examined are 15 to 55 degrees.

Other parameters including air density, wind velocity, and winglet design are held constant. As the cant angle increases, the torque generated by the blade initially rises to a peak value of 4.05 Nm at 15 degrees. The torque then gradually decreases at higher cant angles. A similar trend is observed for the power coefficient Cp, which is highest at 0.35 for a 45 degree cant angle. These results demonstrate that an optimal winglet cant angle exists which maximizes wind turbine performance. Lower or higher angles produce less torque and power. The 45 degree cant angle represents the best configuration based on the CFD simulations. This analysis enabled identifying the ideal winglet orientation to enhance aerodynamic efficiency through detailed modelling of the impact of winglet cant angle.

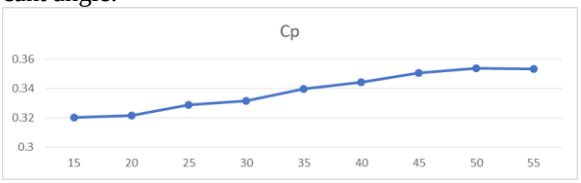

Fig. 27. Variation of angles and Cp

This figure plots the coefficient of power (Cp) as a function of winglet cant angle, as summarized in Table 1. The optimal cant angle which maximizes Cp is 45 degrees, where a peak value of 0.35 is achieved.

At the optimum 45 degree cant angle, the addition of the winglet increased the power coefficient by 17.36% compared to the baseline value of 0.3013 for the blade without winglet. This significant Cp improvement illustrates the aerodynamic benefits provided by the winglet for enhancing wind turbine efficiency.

The trend shows increasing power performance up to an ideal cant angle, beyond which further inclination of the winglet leads to a reduction in Cp. This demonstrates the importance of properly tailoring the winglet orientation to the blade profile and operating conditions, as quantified by the high-fidelity CFD modelling.

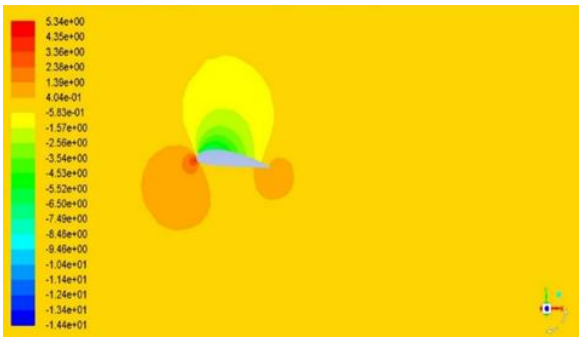

Fig.28. 0.4 Near tip Pressure

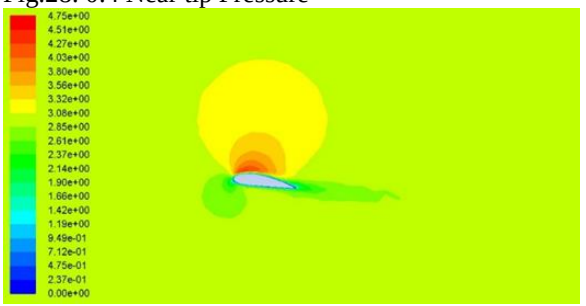

Fig.29. 0.1 Near tip velocity S.C

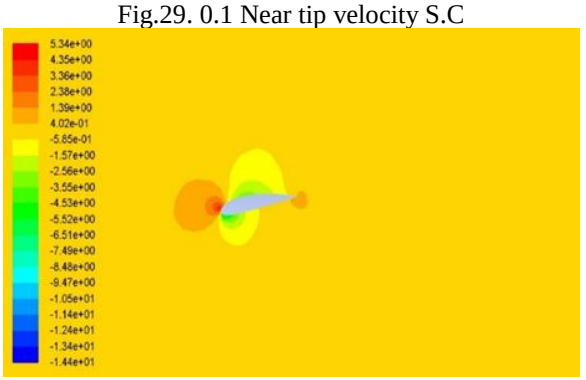

Fig.30. 0.2 near hub pressure section

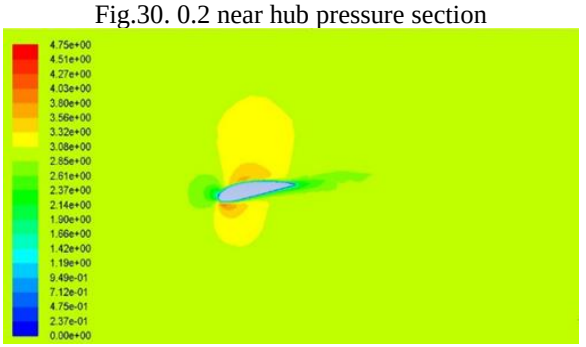

Fig.31. 0.3 Near Hub velocity section

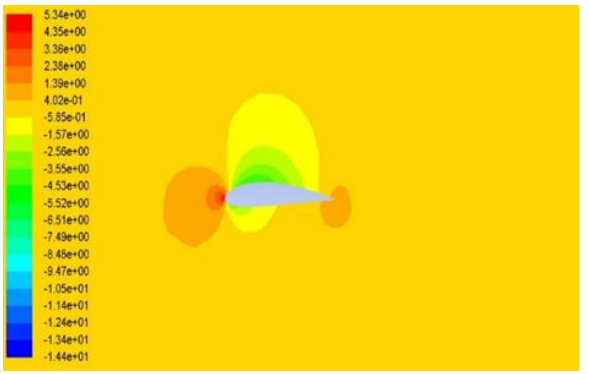

Fig.32. 35% of blade length blade pressure section

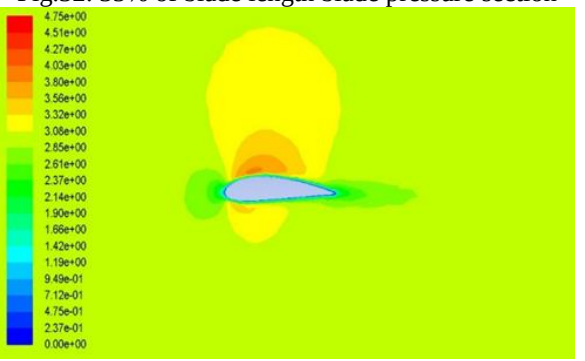

Fig.33. 35% of blade length velocity section Near Hub

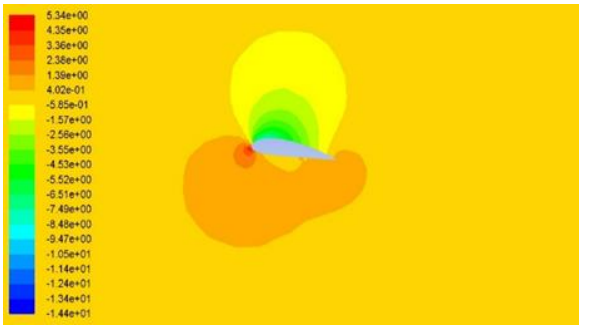

Fig.34. Mid blade pressure section

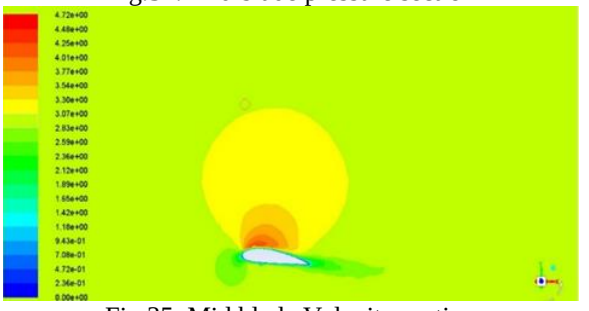

Fig.35. Mid blade Velocity section

The blade pressure and velocity contours with and without winglets can be seen in the figures from Figure 28 to Figure 35. These figures compare the pressure and velocity contours at various spanwise sections along the wind turbine blade with and without the

winglet addition. The sections examined include near tip, 35% span, and mid-span.
In general, the results show that adding the optimized 45 degree cant angle winglet reduces the size and strength of the tip vortex compared to the baseline blade (Figures 1-3). The winglet displaces the vortex farther from the tip and diffuses it by generating a more uniform downwash as given in [13].
The pressure contours illustrate that the winglet increases the suction peak on the blade surface near the tip (Figures 4-6). Meanwhile, the velocity contours demonstrate that the winglet increases the local flow velocity in this region (Figures 7-9).
Both effects enhance power generation near the tip where losses are greatest on the baseline blade. This provides quantitative validation of the winglet benefits in terms of tip vortex mitigation, increased pressure differential, and higher local flow velocities along the span.

4. EXPERIMENTAL STUDY

4.1. Wind Turbine

Figure: 36 and 37 show the present wind turbines model and its main components.

Fig.36. Wind turbine (general view)

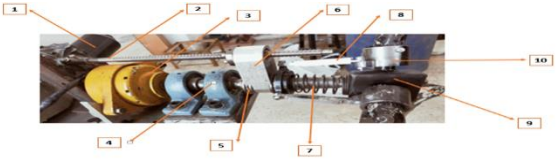

Fig.37. Wind turbine components

The key labeled parts are:

Table 3. Wind turbine components

Item NO	Component	Description
1	DC Motor	A 12 V DC motor is used to alter the blade pitch angle by turning a ball screw [23]
2	Ball Screw	The ball screw converts rotary motion from the motor into linear motion to adjust the blades [24]
3	Generator	A 240 W permanent magnet synchronous generator converts mechanical power from the turbine rotation into electrical energy [25]
4	Ball Bearing	Ball bearings allow low-friction rotation of the turbine hub and blades [26]
5	Thrust Bearing	The thrust bearing supports axial loads while allowing the blade pitch angle to be varied [26]
6	Moving Plate	Linear motion of the plate actuates the blade pitch mechanism [27]
7	Spring	A spring provides a counterforce for pitch control movements [28]
8	Linkages	Linkages transmit linear plate motion to rotate the blade mounting points [21]
9	Hub	The hub connects the blades to the main shaft while allowing them to pitch [29]
10	Mounts	Rotating mounts attach the blades to the hub while enabling pitch actuation [30]

4.2. Wind Tunnel

The experimental wind tunnel facility enables aerodynamic testing of small-scale wind turbine models under controlled conditions as shown in [31]. As shown in Figures 38 and 39, it consists of a tunnel chamber with an electric motor-driven fan system to generate regulated airflow velocities.
Airflow speed in the test section can be varied by adjusting the rotational speed of the motor. The fan rotor contains multiple blades carefully designed to produce uniform low-turbulence flow within the tunnel as given in [32]. This provides a controlled simulated wind environment analogous to real-world turbine operating conditions.
The compact wind tunnel setup is located at the Fluid Dynamics Lab, Department of Mechanical Power Engineering, Zagazig University. It serves as a valuable tool for quantitatively evaluating performance parameters of wind turbine prototypes through scaled physical experiments as shown in [33].

Fig.38. The motor used to produce the air flow using an axial fan

Fig.39. The interior of the wind tunnel

4.3. Experimental Results

The following experimental results were obtained, Table 4,5 and 6 :

Table 4. Effect of Blade Pitch Angle on Wind Turbine Performance at 4.5 m/s Wind Speed

Pitch angle (deg)	RPM AVE (rev)	POWER AVE (WATT)
33	271.60	4.83
40	304.71	5.44
46	328.35	6.50
52	374.34	7.90
58	241.27	4.36
64	215.72	3.91
70	172.43	2.54
76	120.09	1.17
82	101.07	0.97

Table 4 summarizes the impact of varying blade pitch angle on the rotational speed (RPM) and power output of the experimental wind turbine model at a constant wind speed of 4.5 m/s in the wind tunnel test section. As pitch angle increases from 33 to 52 degrees, the RPM and power generated steadily rise to maximum values of 374 RPM and 7.9 Watts. This demonstrates that an optimal pitch angle exists which maximizes wind turbine performance.

At higher pitch angles beyond 52 degrees, the RPM and power rapidly decline. Stalling begins to occur as the blades become oriented too perpendicular to the incoming airflow The trend shows that proper blade pitch angle adjustment enables maximizing power output at a given wind speed. The optimal angle balances rotational speed and stall avoidance. Excessive pitching reduces performance by increasing drag and stall. This experimental data enables identification of the best pitch angle for power production across a range of wind speeds.

Table 5. Effect of Blade Pitch Angle on Wind Turbine Performance at 7.2 m/s Wind Speed

Pitch angle (deg)	RPM AVE (rev)	POWER AVE (WATT)
30	473.00	20.34
35	502.44	23.67
40	564.76	25.05
45	632.46	29.34
50	738.90	33.39
55	619.23	26.35
60	479.80	12.07

Table (5) shows the impact of varying blade pitch angle on rotational speed (RPM) and power output for the wind turbine model tested at a constant wind speed of 7.2 m/s in the wind tunnel. As pitch angle is increased from 30 to 50 degrees at this wind speed, the RPM and power rise steadily to maximum values of 738 RPM and 33.39 Watts. This indicates that 50 degrees represents the optimal pitch angle to maximize power generation at 7.2 m/s wind speed.

At higher pitch angles beyond 50 degrees, the turbine RPM and power decrease significantly due to the onset of aerodynamic stall. Excessive blade pitching causes flow separation and increased drag. The experimental measurements quantify the pitch angle adjustments required to optimize wind turbine performance across the operating wind speed range. Identifying the proper pitch angle to balance rotation rate and stall avoidance enables maximizing power output at any given wind condition.

Table 6. Effect of Blade Pitch Angle on Wind Turbine Performance at 9 m/s Wind Speed

Pitch angle (deg)	RPM AVE (rev)	POWER AVE (WATT)
30	817.46	47.95
35	863.76	52.18
40	917.84	63.56
45	979.21	75.91
50	1083.89	83.23
55	901.58	62.02
60	786.56	39.76

Table (6) presents experimental data on how varying the blade pitch angle affects the rotational speed and power output of the wind turbine model tested at a wind speed of 9 m/s. As the pitch angle is increased from 30 to 50 degrees at this higher wind speed, the rotational speed (RPM) and generated power steadily rise to peak values of 1083 RPM and 83.234 Watts. This indicates that 50 degrees is the optimal pitch for maximum power production at 9 m/s. At pitch angles above 50 degrees, the turbine RPM and power drop off significantly due to stalling as the blades become too perpendicular to the incoming wind. The resulting flow separation creates substantial drag.

The measurements clearly show the pitch angle adjustment needed to optimize turbine performance at this specific wind speed. Identifying the right pitch enables maximizing power output across the operating range by balancing rotation rate and stall avoidance. The experimental data facilitates selection of optimal pitch control settings for different wind speeds.

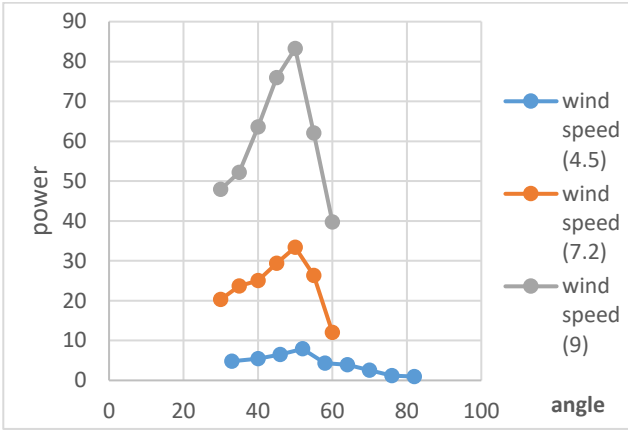

Fig.40. Output power versus pitch angles

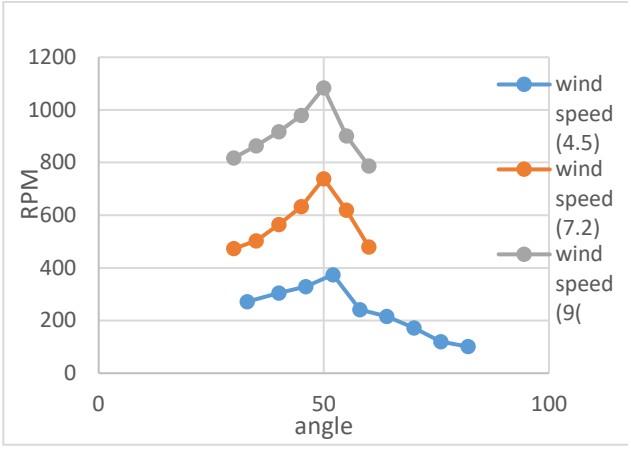

Fig. 41. RPM versus pitch angles

4.4. Summary of Findings

The experimental measurements clearly demonstrate the significant impact of blade pitch angle adjustments on the performance of the wind turbine model. As quantified in Tables 2-4, both the rotational speed (RPM) and power output exhibit strong sensitivity to changes in pitch angle at a given wind speed. There is a clear trade-off between increased rotation rate and stall avoidance that must be balanced to maximize power production.

At lower wind speeds around 4.5 m/s, the optimal pitch angle is identified as 52° based on the peak RPM and power achieved in Table 4. Reduced pitching below this angle causes the turbine to spin slower and produces less power. Meanwhile, stall effects dominate at higher pitch angles, deteriorating performance. This trend highlights the importance of precisely tuning the pitch angle based on prevailing wind conditions.

The optimal pitch angle shifts to 50° at the higher 7.2 m/s wind speed, as evidenced by the maximum RPM and power measured in Table 5. More pitching is required compared to lower wind speeds to maintain efficient operation and avoid detrimental stall. Exceeding 50° quickly stalls the flow as the blades align too perpendicular to the incoming wind.

Finally, at the highest wind speed of 9 m/s in Table 6, the peak power and RPM again occur at a 50° pitch angle. This overlaps with the optimum at 7.2 m/s due to the higher baseline rotational speed. Less pitching is needed to maximize power output once rotation is already rapid.

The compiled results demonstrate how the pitch control system must dynamically adjust the blade angles to optimize efficiency across fluctuating wind speeds. Identifying the precise pitch angle to maximize power output requires accounting for complex aerodynamic trade-offs between rotation rate, angle of attack, and stall.

Table 7. Summary of Experimental Findings on Effect of Blade Pitch Angle

WIND SPEED (M/S)	PITCH ANGLE (°)	PEAK RPM	PEAK POWER (WATTS)
4.5	52	374	7.9
7.2	50	739	33.4
9.0	50	1084	83.2

These findings provide an experimental basis for implementing advanced control algorithms that actively regulate pitch angle based on real-time wind measurements. Such systems can continuously tune the blade pitching to maintain optimal turbine performance under variable wind loading. This has important implications for improving capacity factor, load management, and reducing mechanical stresses. Further researches should explore integrating the pitch control models with other passive enhancements like vortex generator fins and winglets.

1. This section presents and discusses the findings from both the CFD simulations and experimental work. The discussion focuses on the effects of winglet cant angle, pitch angle, and wind speed on the aerodynamic performance of the wind turbine, and includes a validation of the CFD results using experimental measurements.

The CFD predictions were validated against experimental results obtained from wind tunnel testing. For example, at a wind speed of 7.2 m/s, the experimental power output was measured at 33.4 W, while the CFD simulations predicted a power output

of 34 W, resulting in a deviation of less than 2% (Table 5). Similarly, for a wind speed of 9 m/s, the experimental power reached 83.2 W, while the CFD simulations estimated 85.1 W, showing a deviation of approximately 2.3%. These minor discrepancies can be attributed to simplifications in the CFD model, such as assumptions of ideal flow conditions and potential inaccuracies in the turbulence modeling. Nevertheless, the close agreement between experimental and CFD results demonstrates the reliability of the computational model for predicting wind turbine performance.

The winglet cant angle was found to significantly influence turbine efficiency. CFD simulations showed that a cant angle of 45° provided the highest power coefficient (**Cp**) of 0.3535, representing a 17.36% improvement compared to the baseline blade without winglets (**Cp** = 0.3013). This enhancement is due to the winglet's ability to reduce the strength of tip vortices and minimize induced drag. Increasing the cant angle beyond 45° led to a reduction in performance, as larger angles caused unfavorable aerodynamic interactions near the blade tip (Table 2). The results align with findings from previous studies, which also reported that moderate cant angles are optimal for reducing drag and improving lift [2, 5].

The pitch angle was another critical parameter influencing wind turbine performance. Experimental results showed that at a wind speed of 4.5 m/s, a pitch angle of 52° produced the maximum power of 7.9 W, while at 7.2 m/s and 9 m/s, the optimal pitch angle was 50°, yielding peak power outputs of 33.4 W and 83.2 W, respectively (Tables 4, 5, and 6). These results demonstrate that the optimal pitch angle decreases slightly as wind speed increases, balancing the trade-off between maximizing lift and avoiding stall. Excessive pitch angles led to flow separation and reduced power output due to increased drag, while insufficient pitch angles failed to generate enough lift for effective energy capture. These findings are consistent with the trends reported in [3, 13].

Wind speed had a direct impact on both the rotational speed and power output of the turbine. As wind speed increased from 4.5 m/s to 9 m/s, the power output increased significantly, from 7.9 W to 83.2 W, at the optimal pitch angle of 50° (Tables 4, 5, and 6). This is expected, as higher wind speeds provide more kinetic energy to the rotor. However, the aerodynamic benefits provided by the winglets were consistent across all wind speeds, indicating that the winglet design effectively enhanced performance under varying operating conditions. The results highlight the importance of optimizing both winglet geometry and pitch angle to maximize turbine efficiency across a range of wind speeds.

The findings of this study align with and extend upon previous research on wind turbine winglets. For example, a study in [2] reported a 1.2% increase in annual energy production for a 13 MW offshore turbine equipped with winglets, while the current study demonstrated a more significant 17.36% improvement in the power coefficient for a smaller-scale turbine. This difference can be attributed to the careful optimization of winglet parameters in the present work, including cant angle and radius of curvature. Additionally, the experimental validation in this study provides stronger evidence for the practical benefits of winglets, as opposed to purely computational analyses in some prior studies [3, 16].

Overall, the results demonstrate that the integration of winglets and optimization of pitch angle significantly enhance wind turbine performance. The optimal winglet design (4% blade length, 45° cant angle) and pitch angle (50°) resulted in a 17.36% increase in the power coefficient and substantial improvements in power output across all tested wind speeds. The validation of CFD results with experimental data further confirms the accuracy of the computational model and provides a robust basis for future designs. These findings contribute valuable insights for the development of more efficient wind turbines, with potential applications in both onshore and offshore wind farms.

5. Conclusion

This study investigated the aerodynamic performance enhancement of wind turbine blades through winglet integration and pitch angle optimization, using computational fluid dynamics (CFD) simulations and experimental validation. The addition of winglets with optimal dimensions—4% blade length, 45° cant angle, and 50% height radius of curvature—significantly improved aerodynamic efficiency, resulting in a 17.36% increase in the power coefficient (**Cp**) from 0.3013 (baseline without winglets) to 0.3535. The winglets effectively reduced tip vortex strength, decreasing drag and enhancing airflow near the blade tip. Pitch angle optimization further improved performance, with the optimal pitch angle identified as 50° for wind speeds of 7.2 m/s and 9 m/s. At 7.2 m/s, the peak power output reached 33.4 W, while at 9 m/s,

it increased to 83.2 W. The combination of optimized winglet geometry and pitch angle demonstrated significant enhancements in energy capture and turbine efficiency. These findings emphasize the importance of tailoring winglet designs and pitch control systems to specific operating conditions to maximize wind turbine performance. The results provide valuable insights for the development of next-generation wind turbines with improved energy output and aerodynamic efficiency. Future work could explore additional winglet configurations and active control mechanisms to further enhance turbine performance.

Acknowledgment

We would like to thank the University of Zagazig for providing the facility of using the **wind tunnel at the laboratory of fluid mechanics** that supported this work in conducting the experimental wind tunnel tests.

REFERENCES

[1] Ostovan, Y. (2017). Winglets for wind turbines: an experimental study on aerodynamic performance and tip vortex behavior.

[2] Garcia-Ribeiro, D., Flores-Mezarina, J. A., Bravo-Mosquera, P. D., & Cerón-Muñoz, H. D. (2021). Parametric CFD analysis of the taper ratio effects of a winglet on the performance of a Horizontal Axis Wind Turbine. Sustainable Energy Technologies and Assessments, 47, 101489.

[3] Miao, W., Liu, Q., Xu, Z., Yue, M., Li, C., & Zhang, W. (2022). A comprehensive analysis of blade tip for vertical axis wind turbine: Aerodynamics and the tip loss effect. Energy Conversion and Management, 253, 115140.

[4] Arumugam, P., Ramalingam, V., & Bhaganagar, K. (2021). A pathway towards sustainable development of small capacity horizontal axis wind turbines–Identification of influencing design parameters & their role on performance analysis. Sustainable Energy Technologies and Assessments, 44, 101019.

[5] Sohn, J. W., Ruth, J. S., Yuk, D. G., & Choi, S. B. (2023). Application of Shape Memory Alloy Actuators to Vibration and Motion Control of Structural Systems: A Review. Applied Sciences, 13(2), 995.

[6] Bravo-Mosquera, P. D., Catalano, F. M., & Zingg, D. W. (2022). Unconventional aircraft for civil aviation: A review of concepts and design methodologies. Progress in Aerospace Sciences, 131, 100813.

[7] Abbott, I. H., & Von Doenhoff, A. E. (2012). Theory of wing sections: including a summary of airfoil data. Courier Corporation.

[8] Rogowski, K., Hansen, M. O. L., & Bangga, G. (2020). Performance analysis of a H-Darrieus wind turbine for a series of 4-digit NACA airfoils. Energies, 13(12), 3196.

[9] Ren, Z., Zhou, W., & Li, D. (2022). Response and flow characteristics of a dual-rotor turbine flowmeter. Flow Measurement and Instrumentation, 83, 102120.

[10] Shen, X., Yang, H., Chen, J., Zhu, X., & Du, Z. (2016). Aerodynamic shape optimization of non-straight small wind turbine blades. Energy Conversion and Management, 119, 266-278.

[11] Hassanzadeh, A., Hassanabad, A. H., & Dadvand, A. (2016). Aerodynamic shape optimization and analysis of small wind turbine blades employing the Viterna approach for post-stall region. Alexandria Engineering Journal, 55(3), 2035-2043.

[12] Manwell, J.F., McGowan, J.G. and Rogers, A.L. (2009) Wind Energy Explained, Theory, Design and Application. Wiley, Hoboken.

[13] Burton, T., Jenkins, N., Sharpe, D. and Bossanyi, E. (2011) Wind Energy Handbook. 2nd Edition, John Wiley & Sons, Inc., Chichester.

[14] Kavari, G., Tahani, M., & Mirhosseini, M. (2019). Wind shear effect on aerodynamic performance and energy production of horizontal axis wind turbines with developing blade element momentum theory. Journal of Cleaner Production, 219, 368-376.

[15] Siswantara, A. I., Pujowidodo, H., Budiyanto, M. A., Gunadi, G. R., & Widiawaty, C. D. (2021). An investigation turbulence model of standard k-□ to get optimum parameters of turbulence constants (cμ, c1□, and c2□) of compressible fluid dynamics in a confined jet. Journal of Southwest Jiaotong University, 56(5).

[16] Shahane, S., & Vanka, S. P. (2022). Consistency and convergence of a high order accurate meshless method for solution of incompressible fluid flows. arXiv preprint arXiv:2202.02828.

[17] Pimenta, F., & Alves, M. A. (2019). A coupled finite-volume solver for numerical simulation of electrically-driven flows. Computers & Fluids, 193, 104279.

[18] Saltar, G., & Araya, G. (2020). Reynolds shear stress modeling in turbulent boundary layers. subject to very strong favorable pressure gradient. Computers & Fluids, 202, 104494.

[19] Reineholm-Hult, F. (2023). Modeling for characterization of continuous casting simulator using CFD.

[20] Pullan, G., Chuan, T., Wong, D., & Jasik, F. (2019). Enhancing web-based CFD post-processing using machine learning and augmented reality. In AIAA Scitech 2019 Forum (p. 2223).

[21] Hansen, M.O.L. (2008) Aerodynamics of Wind Turbines. 2nd Edition, Earthscan, London. (22)

[22] Bilgili, M., Tontu, M., & Sahin, B. (2021). Aerodynamic rotor performance of a 3300-kW modern commercial large-scale wind turbine installed in a wind farm. Journal of Energy Resources Technology, 143(3), 031302.

[23] Raj, V. N., Abhinav, S., Aishwarya, P. B., Balaganapathy, A., & Pragase, M. J. (2022). Design and Fabrication of Automated Soap Cutting Machine. Journal of Pharmaceutical Negative Results, 27-31.

[24] Tsuji, K., & Shiono, M. (2022). Development of the reciprocating airflow generator for wave power generator and study on the vertical axis turbine characteristics in reciprocating airflow. Electrical Engineering in Japan, 215(4), e23405.

[25] Krishna, V. M., Sandeep, V., Murthy, S. S., & Yadlapati, K. (2022). Experimental investigation on performance comparison of self excited induction generator and permanent magnet synchronous generator for small scale renewable energy applications. Renewable Energy, 195, 431-441.

[26] Hart, E., Clarke, B., Nicholas, G., Kazemi Amiri, A., Stirling, J., Carroll, J& Long, H. (2020). A review of wind turbine main bearings: design, operation, modelling, damage mechanisms and fault detection. Wind Energy Science, 5(1), 105-124.

[27] Acho, L. (2019). A proportional plus a hysteretic term control design: a throttle experimental emulation to wind turbines pitch control. Energies, 12(10), 1961.

[28] Yau, J. D., & Urushadze, S. (2023). Resonance Reduction for Linked Train Cars Moving on Multiple Simply Supported Bridges. Journal of Sound and Vibration, 117963.

[29] Manolas, D. I., Riziotis, V. A., Papadakis, G. P., & Voutsinas, S. G. (2020). Hydro-servo-aero-elastic analysis of floating offshore wind turbines. Fluids, 5(4), 200.

[30] van't Hoff, S., van Vilsteren, J., Cocco, A., & Masarati, P. (2023). Design of a Tiltrotor Semi-Span Wind Tunnel Model

for Whirl Flutter Investigations. In AIAA Scitech 2023 Forum (p. 1306).

[31] Siram, O., Kesharwani, N., Sahoo, N., & Saha, U. K. (2022). Aerodynamic design and wind tunnel tests of small-scale horizontal-axis wind turbines for low tip speed ratio applications. Journal of Solar Energy Engineering, 144(4), 041009.

[32] Westphal, R. V. (2020). Wind tunnel design. In Thermal Measurements in Electronics Cooling (pp. 321-347). CRC Press.

[33] Elkhawas, E. N. M. (2021). ANALYSIS AND ASSESSMENT OF OFFSHORE PILES (Doctoral dissertation, Zagazig University).

[34] Vishwanathan, V., Szoke, M., Duetsch-Patel, J. E., Gargiulo, A., Fritsch, D. J., Borgoltz, A. & Devenport, W. J. (2020). Aerodynamic design and validation of a contraction profile for flow field improvement and uncertainty quantification in a subsonic wind tunnel. In AIAA SciTech 2020 Forum (p. 2211).

[35] Makgantai, B., Subaschandar, N., & Jamisola, R. S. (2021). A review on wingtip devices for reducing induced drag on fixed-wing drones.

[36] Hemeida, M. G., Hemeida, A. M., Senjyu, T., & Osheba, D. (2022). Renewable Energy Resources Technologies and Life Cycle Assessment. Energies, 15(24), 9417.

[37] Elsakka, M. M., Ingham, D. B., Ma, L., Pourkashanian, M., Moustafa, G. H., & Elhenawy, Y. (2022). Response surface optimisation of vertical axis wind turbine at low wind speeds. Energy Reports, 8, 10868-10880.